Nonlocal Independent Pixel Approximation: Direct and Inverse Problems

Alexander Marshak, Anthony Davis, Robert F. Cahalan, and Warren Wiscombe

Abstract— The independent pixel approximation (IPA), which treats radiative properties of each pixel independently by using standard plane-parallel calculations preserves scale-invariance found in the analyses of the horizontal variability of liquid water in marine stratocumulus clouds. Several studies, however, report a violation of scale-invariance in LANDSAT cloud radiance fields that are much smoother than cloud structure on small scales. This shows a limitation of IPA on small scales: it is unable to simulate the smooth small-scale behavior that is due to the horizontal photon transport. This paper introduces a "nonlocal" independent pixel approximation (NIPA) that extends the IPA by incorporating empirically the smoothing effects of horizontal interpixel fluxes through a convolution product of the IPA and an approximate Green function for radiative transfer. We also address the inverse problem of cloud optical depth retrieval from satellite data, showing how NIPA can be used to overcome the limitations of current IPA-based methods at small scales.

I. INTRODUCTION

ACCURATE retrieval of cloud optical properties from satellite data is one of the main problems of cloud remote sensing. The large number of cloud types with different vertical and horizontal variability in cloud optical properties makes this problem very difficult and the retrieved optical depth fields in some cases unreliable. Many studies address the problem of uncertainties in the retrieval of visible wavelength optical depth from satellite measurements [1]–[5]. These discuss uncertainties arising from inaccurate knowledge of illumination geometry, cloud aspect ratio, single-scattering albedo, scattering phase function, surface albedo, vertical structure of clouds, and calibration/discretization. A review of uncertainties in cloud optical depth retrieval was done in [6]. Recently [7], systematic biases in the retrieved optical depths were found for thick clouds at oblique solar zenith angles.

The existing retrieval techniques are entirely one-dimensional, assuming horizontal homogeneity below the pixel-scale, and based on look-up tables [2], [3], [8].

According to [9], these are an operational independent pixel approximation (IPA), where radiation fields are computed on a pixel-by-pixel basis with plane-parallel theory. In other words, IPA is a standard plane-parallel radiative transfer model weighted by the probability distributions of the various cloud properties. For the large enough scales (e.g., averaged over several tens of kilometers) and completely overcast skies, IPA is a reasonable approximation. Recently [10], domain-averaged properties of IPA have been improved by including the actual spatial distribution of the direct solar transmission as the source term in otherwise one-dimensional (1-D) computations. If the distribution of cloud optical depth is approximated by the gamma distribution [11], an analytical expression for the domain-averaged radiative fluxes can be derived for both conservative and nonconservative scattering [12]. This method is called a gamma-IPA model. The gamma function parameter can be used to fit the histograms of IPA-retrieved cloud optical depth [13].

Because IPA performs plane-parallel calculations for each pixel, it neglects the net horizontal fluxes excited by the spatial variability. As a result, dramatic errors in individual pixel radiances that can exceed 50% [14], [15] even for high solar zenith angles. These errors lead to large discrepancies in local optical depth, retrieved by inverting the IPA at scales smaller than 0.5–1 km [16].

On the other side, Monte Carlo (MC) methods are accurate but computationally costly when pixel-scale resolution is required; furthermore, they do not give one-to-one radiance/optical depth relations. Up to now there is nothing that combines the accuracy of MC with speed and straightforward invertability of IPA. The method proposed in this paper fills this gap. We call it the nonlocal independent pixel approximation (NIPA) because it is not limited to the local values of optical thickness τ but takes into account horizontal radiative fluxes. It has recently been realized theoretically [15] and verified empirically [16] that these horizontal fluxes are dictated by a specific process called "radiative smoothing" mediated by multiple scattering. Radiative smoothing is incorporated into NIPA empirically through a convolution product of the IPA and the cloud's radiative Green function, which characterizes the spot of diffusely reflected light resulting from illumination by a narrow beam [16].

There are several limitations of NIPA in the present study. First, the interpixel correction remains independent of solar angles and thus of geometrical shadows (see [7] for the effect of solar zenith angles on the retrieved optical depths). Second, NIPA is unable to simulate albedos larger than unity:

due to converging horizontal fluxes, more energy leaves the corresponding pixel than enters it. This is not a rare occurrence for low sun and highly variable clouds [15], [17]. Third, we assume vertical homogeneity. The geometrical shadowing, however, may have a large effect for clouds with vertical inhomogeneity [18]. Finally, we assume that each pixel is either completely filled with a single uniform cloud layer or else it is clear.

In this study, we constrain ourselves with overcast clouds having constant top and base. The only variable quantity is the horizontal distribution of optical thickness τ. This simple model corresponds most closely to marine stratocumulus (Sc), typically a few hundred meters thick and at least several hundred kilometers across with approximately horizontal upper boundary. Based on passive microwave observations [19], a simple fractal model of the horizontal variability of optical thickness that simulates internal cloud structure was developed [20]. The main property of this model is the power-law behavior of its wavenumber spectrum

$$E(k) \propto k^{-\beta}, \qquad k = |\boldsymbol{k}| = (k_1^2 + k_2^2)^{1/2} \qquad (1)$$

over a large range of scales $r = 1/k$. Davis *et al.* [21], [22] indeed found such power-law spectra for liquid water fluctuations in marine Sc, with r in a range from several tens of meters to tens of kilometers.

The plan of this paper is as follows. The next section briefly describes our fractal cascade models that reproduce the scaling properties of measured cloud liquid water. Section III compares two methods of computing radiation fields (IPA and MC) and shows the results of a numerical experiment where net horizontal fluxes are estimated directly inside inhomogeneous clouds. In Section IV, we describe a direct NIPA and compare it with both MC and IPA. Finally, Section V sets up the inverse problem of deconvolution and shows how this ill-posed problem can be regularized to obtain a stable solution for the retrieved optical depth field. Section VI summarizes the results and discusses their applicability.

II. HORIZONTAL DISTRIBUTION OF CLOUD OPTICAL DEPTH

Both *in situ* measurements of liquid water content [21], [22] and ground-based measurements of liquid water path [19], [23] indicate power-law behavior of the horizontal variability of cloud structure over at least three orders of magnitude: from several tens of meters to tens of kilometers. This means that a plot of any well-defined measure of variability (variance, standard deviation, wavenumber spectrum, etc.) versus scale in a log–log plot produces a straight line. For example, a log–log plot of wavenumber spectrum $E(k)$ versus k in (1) gives a slope $-\beta$, which is invariant under changes in wavenumber k. Similarly, for the incremental standard deviation σ_ϕ of a field ϕ one can write

$$\sigma_\phi(r) = \sqrt{\langle |\phi(\boldsymbol{x}) - \phi(\boldsymbol{x} + \boldsymbol{r})|^2 \rangle} \propto |\boldsymbol{r}|^H = r^H \qquad (2)$$

where $\langle \cdot \rangle$ denotes ensemble averaging and the exponent H is invariant under changes in scale r; it is defined by the slope of a straight line in a log σ_ϕ versus log r plot. (The Wiener–Khinchine theorem [24] for scale-invariant stochastic
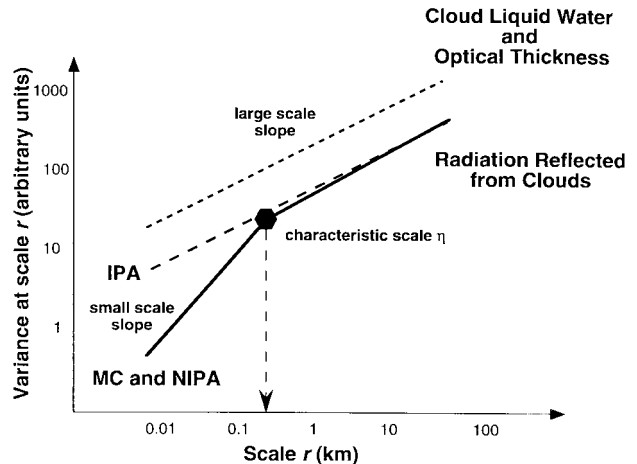

Fig. 1. A schematic log–log plot of variance at a given scale versus that scale. Vertically we represent the wavenumber spectrum or the incremental variance. The plot shows (scale-invariant) cloud liquid water data along with two computed radiation fields, IPA and MC/NIPA. The latter, showing a scale-break at the "radiative smoothing" scale $\eta \approx 100$–300 m for marine stratocumulus clouds, agrees with LANDSAT observations. The IPA curve depends only on the cloud optical depth field and thus is slaved to it, showing no scale-break.

processes tells us that the two exponents β and H are related as $\beta = 2H + 1$.) The upper line in Fig. 1 schematically illustrates the scale-invariant behavior of cloud liquid water.

Different fractal models have been proposed to simulate cloud inhomogeneity [20], [25], [27]. For the purposes of this study, we employ two-parameter bounded cascade model [20], [26], which mimics the wavenumber spectrum (1) and variance of log of observed cloud liquid water in marine Sc. This model assumes that clouds have fixed upper and lower boundaries; cloud optical thickness is homogeneous in the vertical direction and varies only horizontally. Fig. 2 shows a perspective plot of this model in two-dimensions (2-D).

III. INDEPENDENT PIXEL APPROXIMATION AND MONTE CARLO

Perhaps the simplest way to study the radiation properties of horizontally inhomogeneous clouds is to apply the IPA, i.e., plane-parallel theory on a pixel-by-pixel bases. In other words, *net* horizontal photon transport is neglected, and each pixel is treated as an independent plane-parallel medium, when only local optical depth varies. To compute an IPA reflection for each local value of optical thickness, one can use either generalized two-stream formulae (e.g., [9]) or, more accurately, any numerical technique developed for a plane-parallel medium (e.g., DISORT routines described in [28]).

For our purposes, the most important property of IPA is the preservation of scaling. In other words, if the optical thickness field is scale-invariant, as in (2), then, to a first approximation, the resulting IPA radiation field R_{IP} is also scale-invariant [16] and

$$\sigma_{\mathrm{IP}}(r) = \sqrt{\langle |R_{\mathrm{IP}}(\boldsymbol{x}) - R_{\mathrm{IP}}(\boldsymbol{x} + \boldsymbol{r})|^2 \rangle}$$
$$\propto \sqrt{\langle |\tau(\boldsymbol{x}) - \tau(\boldsymbol{x} + \boldsymbol{r})|^2 \rangle} \propto r^H, \qquad r = |\boldsymbol{r}|. \quad (3)$$

The middle line in Fig. 1 schematically shows scale-invariance of the IPA. As it follows from (3), this line is parallel to the
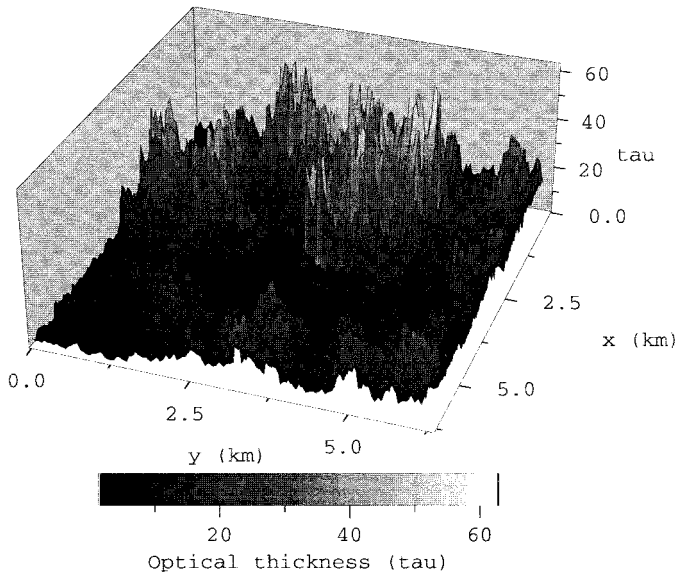
Fig. 2. A 2-D bounded cascade model of optical thickness with seven discrete cascade steps (128 × 128 pixels). Described in [20] and [29], it realistically simulates a rich cloud structure with only two adjustable parameters. The first parameter (p) controls the variance-to-mean ratio of cloud liquid water while the second one (H) defines its scaling behavior. The choice of parameters are made according to [9]: $p = 0.4$ and $H = 0.38$; the latter gives a spectral exponent $\beta \approx 1.6$, roughly that observed for cloud liquid water [21], [22]. The average optical thickness $\langle \tau \rangle$ is set to 13; this yields the standard deviation $\sigma_\tau = 8.9$.

cloud liquid water one and both straight lines are uniquely defined by the same slope H.

One consequence of scaling preservation can also be seen by comparing Fig. 3(a) and (c), respectively, grayscale renderings of $\tau(x_1, x_2)$ and $R_{\mathrm{IP}}(x_1, x_2)$ 2-D fields. The sharp edges in the τ field result from the discrete nature of the cascade model used to generate optical depth fluctuations [29]; because it is slaved to τ-field, the R_{IP}-field shows the same sharp features.

Another way of computing radiation reflected from horizontally inhomogeneous clouds is by Monte Carlo (MC) simulations—a robust but rather costly technique that uses photon trajectories with given probability densities, defined by the integral equation of radiative transfer [30]. Fig. 3(b) shows the 2-D albedo field $R_{\mathrm{MC}}(x_1, x_2)$ calculated by MC [29] for the τ-field in panel 3a. Even visually, we see that this R_{MC} is much smoother than R_{IP} in Fig. 3(c). At largest scales, the discreteness of the model is still perceptible, i.e., the large-scale fluctuations of the optical thickness field τ are preserved. At small scales, however, the edges are smoothed by the horizontal fluxes. This reflects the fact that R_{MC} is no longer scale-invariant, and the lower part of the broken line in Fig. 1 defines a characteristic scale η separating the two regimes. For scales above η, radiation follows the fluctuations in cloud structure while, for scales below η, the radiation field is smoother than predicted.

Scale-by-scale analyses of cloudy LANDSAT scenes [16], [19], [33] show a scale break at around 200 m. We plotted in Fig. 4(a) and (b), respectively, wavenumber spectra $E(k)$ and standard deviations $\sigma(r)$ of the July 7, 1987, LANDSAT marine Sc scene of 61 × 61 km^2 for two weakly-absorbing channels: band 2 (0.52–0.60 μm) and band 4 (0.76–0.90 μm).

We can clearly see a scale-invariant regime from about 0.2–8 km. The scale-break at $\approx$8 km marks the decay of spatial correlations at the "integral" scale [16], [22]. The transition to a steeper slope at around 0.2 km indicates the onset of the radiative smoothing at scale η. Comparison with other cloudy LANDSAT images (e.g., [16]) shows that the large-end scale break changes from image to image while the small-end scale break is quite robust.

Based on the diffusion approximation, η is found to be given [15], [16] by

$$\eta \approx \frac{h}{\sqrt{(1 - g)\langle \tau \rangle}} \qquad (4)$$

where h and $\langle \tau \rangle$ are, respectively, geometrical and (mean) optical cloud thickness and g is the asymmetry factor. For typical marine Sc, $h = 0.3$ km, $\langle \tau \rangle = 13$, and $g = 0.85$; equation (4) then yields $\eta \approx 0.2$ km, which is close to the one observed in Fig. 4(a) and (b).

The IPA provides a reasonable estimate of the radiative properties at large scales [9], [29]; however, because it ignores any horizontal photon transport, there is a dramatic difference for small scales that can be in error by 50% or more (e.g., [15], [17]). To measure the magnitude of the net horizontal fluxes excited by horizontal inhomogeneity, we set up the following numerical experiment. A homogeneous slab of 300 m depth is divided into two parts: one is set to the optical thickness 30 and the other to 5. A backward Monte Carlo [30] was used to simulate separately vertical and horizontal fluxes at different levels. Sun was in zenith to eliminate any effect of geometrical shadowing. Fig. 5 illustrates the results "measured" at 15 m from the discontinuity, in the more tenuous region. For the homogeneous case ($\tau_{\mathrm{thin}} = \tau_{\mathrm{thick}} = 30$), the net vertical fluxes (the straight line at 0.775) are computed using DISORT [28] and the net horizontal fluxes (noisy line around 0) using MC; the latter shows the level of MC errors. The net horizontal flux is of course directed toward the thinner region; its maximum is reached about 50 m from cloud top, which is close to one transport mean free path in the dense region $h/(1 - g)\tau \approx 67$ m. Near cloud bottom, the effect of horizontal fluxes is minimal. The most interesting fact is that the maximum value of net horizontal fluxes is about 30% of their vertical counterpart for the gradient between thick and thin regions of 25, which is not a rare event in horizontal variations in optical depth of real marine Sc [19]. It has also been noticed [17] that for nonabsorbing wavelengths the sum of albedo and transmittance on a pixel-by-pixel bases can be different from unity by up to 30–50%.

To summarize, ignoring net horizontal radiative fluxes for horizontally variable clouds yields incorrect radiation fields for scales on the order of—or smaller than—the smoothing scale η. Fig. 1 illustrates this schematically using scale-by-scale analysis. To incorporate the effect of photon horizontal transport in a simple IPA-type radiative transfer method, one has to find a nonlinear transformation, which "bends" the slope of variance on a log–log plot toward less variability at the smallest scales. The next section shows such a transformation as a convolution product of IPA with an approximate Green function for radiative transfer.
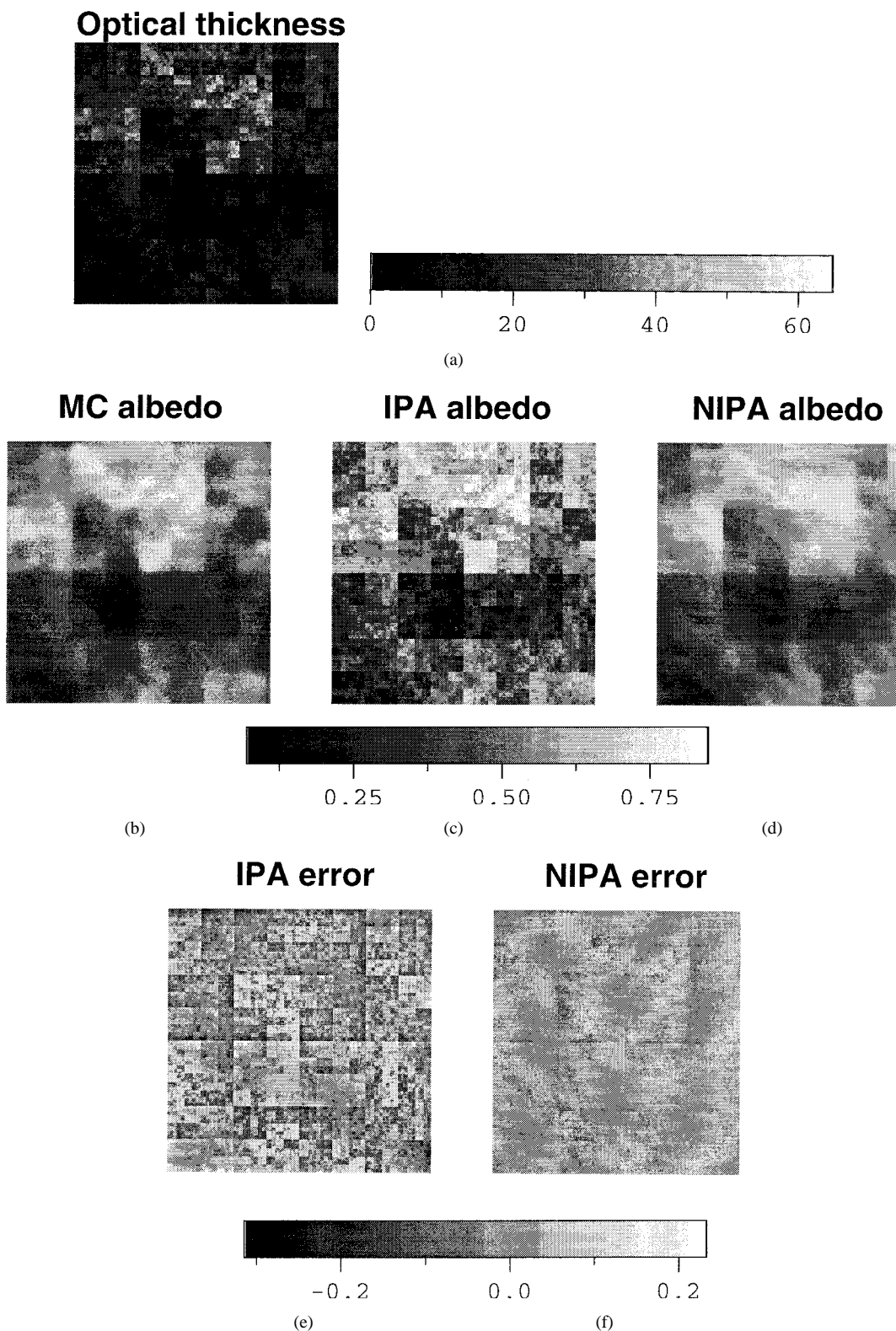
Fig. 3. A 2-D optical thickness, albedo, and albedo-error fields. (a) Density plot of the optical thickness model in Fig. 2. Optical thickness varies from 1.4 to 63. Cloud geometrical thickness $h = 300$ m and the horizontal grid size is 128×128 with 50 m pixels. (b) R_{MC} for sun at 22.5° (from the north) and Henyey–Greenstein phase function with $g = 0.85$. R_{MC} varies from 0.14 to 0.83 with mean $\langle R_{MC} \rangle = 0.46$, and standard deviation $\sigma_{R_{MC}} = 0.14$. The grayscale goes from 0.07 (black) to 0.85 (white). (c) R_{IP} for the same conditions as in (b). It varies over the full grayscale from 0.07 to 0.85 with $\langle R_{IP} \rangle \approx \langle R_{MC} \rangle$, and $\sigma_{R_{IP}} = 0.17 > \sigma_{R_{MC}}$. (d) R_{NIP} with $\alpha = 1.5$ and $\eta = 0.0205$ km for the same conditions as in (b) and (c). It varies from 0.13 to 0.77 with $\langle R_{NIP} \rangle = \langle R_{IP} \rangle \approx \langle R_{MC} \rangle$, and $\sigma_{R_{NIP}} = 0.14 \approx \sigma_{R_{MC}}$. The grayscale is the same as in (b) and (c). (e) $R_{MC} - R_{IP}$ varies from -0.31 to 0.23 with $\langle R_{MC} - R_{IP} \rangle = 0.0016$ and $\sigma_{R_{MC} - R_{IP}} = 0.0669$. The grayscale covers the full range, from -0.31 to 0.23. (f) $R_{MC} - R_{NIP}$ varies from -0.11 to 0.10 with $\langle R_{MC} - R_{NIP} \rangle = \langle R_{MC} - R_{IP} \rangle$, and $\sigma_{R_{MC} - R_{NIP}} = 0.0205 \approx \sigma_{R_{MC} - R_{IP}} / 3$. The grayscale is the same as in panel e.
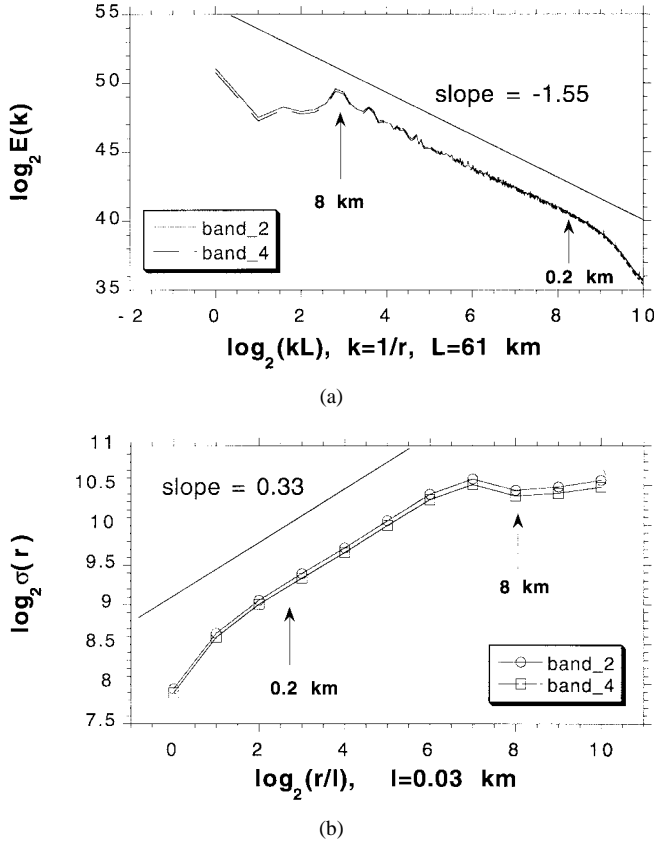
Fig. 4. Wavenumber spectra and standard deviations for a Landsat marine Sc scene of 61×61 km^2 from July 7, 1987. (a) Log–log plot of 2-D wavenumber spectra for two bands: band 2 (0.52–0.60 μm) and band 4 (0.76–0.90 μm). (b) For the same bands, log–log plot of standard deviation $\sigma(r) = \sqrt{\langle |R(x_1 + r, x_2) - R(x_1, x_2)|^2 \rangle}$, averaged over 2048 stripes in the y-direction. Two positions of 8 and 0.2 km are indicated with arrows. Note the small-scale break around 100–200 m.

IV. NONLOCAL INDEPENDENT PIXEL APPROXIMATION: THE DIRECT PROBLEM

As illustrated in Fig. 1, R_{IP} is scale-invariant and the scaling of its variability is therefore defined by just one exponent H [see (3)] over the full range of scales. In contrast, to describe the scaling properties of R_{MC}, one needs at least two more parameters. There is another exponent α, which determines small-scale behavior in Fig. 1 [and/or Fig. 4(a) and (b)] and the characteristic scale η, which defines the scale break. Thus to "simulate" the scaling properties of R_{MC} with R_{IP}, we can convolve the latter with a two-parameter smoothing kernel. Studying numerically the profile of the "spot" of reflected light associated with a point-wise source (the cloud's Green function), it was found [15] that a gamma-type distribution is a good candidate for this convolution product.

Let

$$
\begin{aligned}
G(\alpha, \eta; \boldsymbol{x}) &= G(\alpha, \eta; x_1, x_2) \\
&= c(x_1^2 + x_2^2)^{(\alpha-1)/2} \exp\left[-\frac{\alpha(x_1^2 + x_2^2)^{1/2}}{\eta} \right] \\
&\quad \alpha > 0, \eta > 0
\end{aligned}
\tag{5}
$$

where c is a normalization constant, be a two-parameter gamma-type distribution, which approximates the cloud's ra-
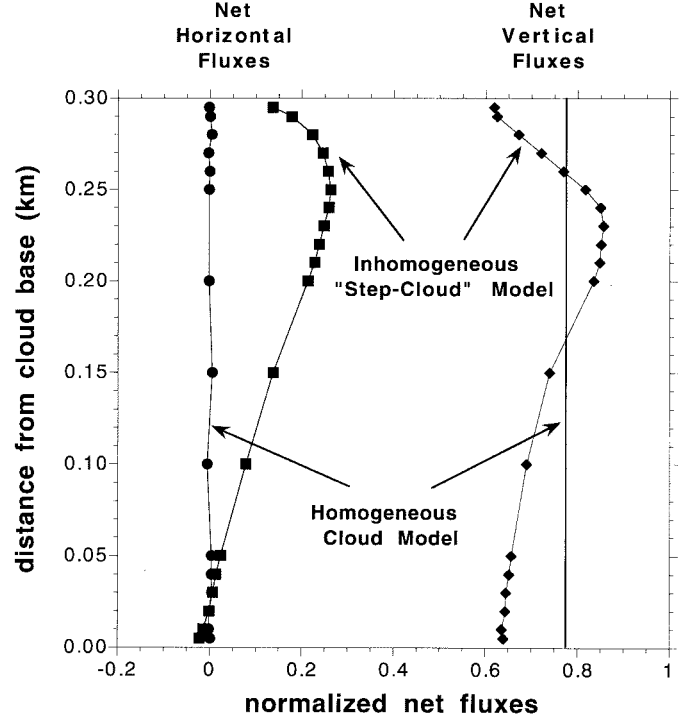

Fig. 5. Net horizontal and vertical fluxes. A homogeneous cloud layer 300 m thick was divided into two regions with optical thicknesses 30 and 5. Point-wise fluxes were calculated using backward MC at 15 m from the discontinuity in extinction. Sun was in zenith and a Henyey–Greenstein phase function with $g = 0.85$ was used. Net fluxes are defined as the differences between down and up fluxes (net vertical) and right and left fluxes (net horizontal). A straight line at 0.775 is computed using DISORT [28] and corresponds to the net (constant) vertical flux in a homogeneous medium with $\tau = 5$. The noisy line at 0 is net horizontal flux in homogeneous medium of $\tau = 5$ computed by backward MC. Note that, near cloud top, net horizontal flux exceeds 30% of net vertical flux.

diative transfer Green function [34]. We define the "nonlocal independent pixel approximation" (NIPA) as the 2-D convolution product of $R_{\text{IP}}(\boldsymbol{x})$ with $G(\alpha, \eta; \boldsymbol{x})$, i.e.,

$$
R_{\text{NIP}}(\boldsymbol{x}) = G(\alpha, \eta; \boldsymbol{x}) * R_{\text{IP}}(\boldsymbol{x}), \qquad \boldsymbol{x} = (x_1, x_2). \tag{6}
$$

Fig. 3(d) illustrates R_{NIP}; it is almost indistinguishable from R_{MC} plotted in Fig. 3(b). From the other side, visual comparison between R_{NIP} [Fig. 3(d)] and R_{IP} [Fig. 3(c)] indicates that, while the large-scale variability of NIPA and IPA [i.e., the distribution of *big* bright and dark areas in Fig. 3(c) and (d)] is very similar, the small-scale fluctuations are quite different. Because of the dampening effect of the convolution product in (6), R_{NIP} is much smoother. In [15] it is shown that, for scales larger than η, wavenumber spectra $E(k)$ of R_{NIP} and R_{IP} are alike; the small-scale spectrum of R_{NIP}, however, has a much steeper slope, which is determined by α and η. Fig. 3(e) and (f) show errors of both methods with respect to R_{MC}. Due to the normalization in (5), R_{NIP} and R_{IP} have the same spatial mean; thus

$$
\langle R_{\text{MC}} - R_{\text{NIP}} \rangle = \langle R_{\text{MC}} - R_{\text{IP}} \rangle = 0.0016. \tag{7a}
$$

The standard deviation σ of the difference $R_{\text{MC}} - R_{\text{NIP}}$ however is more than three times smaller than for $R_{\text{MC}} - R_{\text{IP}}$, more precisely

$$
\sigma_{R_{\text{MC}} - R_{\text{NIP}}} = 0.0205, \quad \sigma_{R_{\text{MC}} - R_{\text{IP}}} = 0.0669. \tag{7b}
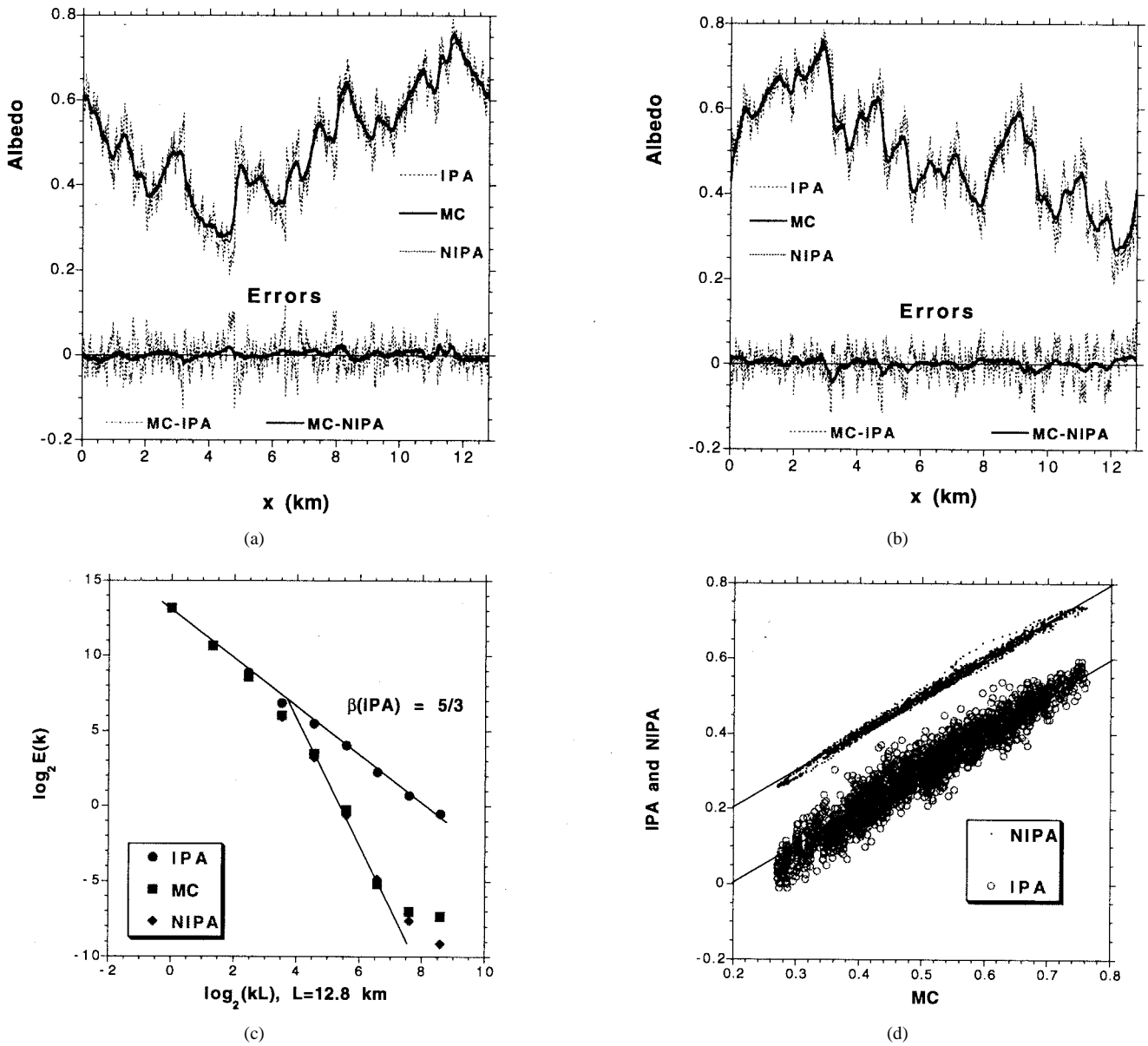$$

Fig. 6. IPA, MC and NIPA for cloud albedos. (a) R_{IP}, R_{MC}, and R_{NIP} ($\eta = 0.115$ km, $\alpha = 1.0$) applied to a 1-D cloud model (plotted in Fig. 8) based on a ten-step bounded cascades ($2^{10} = 1024$ pixels). The differences $R_{MC} - R_{IP}$ and $R_{MC} - R_{NIP}$ are added for better visualization. The average optical thickness $\langle\tau\rangle = 13$ and geometrical thickness $h = 300$ m. The horizontal pixel size is set to 12.5 m, hence, an outer-scale of 12.8 km. Solar zenith angle $\theta_0 = 22.5°$ and azimuthal angle $\varphi_0 = 0°$ (illumination from the left); scattering is determined by a Henyey–Greenstein phase function with $g = 0.85$. (b) The same as in (a) but for another realization (the same as in [15]) of bounded model. (c) Energy spectra of the three fields from (a) and (b) averaged over two realizations. Compare with the schematic illustration in Fig. 1. (d) Scatter plot of IPA and NIPA albedos versus MC albedo for two realizations from (a) and (b). For clarity, R_{IP} results are shifted down by 0.2.

The improvement can be visualized even more clearly in a 1-D case. Fig. 6(a) and (b) show R_{MC}, R_{IP} and R_{NIP} ($\eta \approx 0.12$ km and $\alpha = 1.0$) for two different realizations of a 1-D bounded model with ten cascades. (The main statistics of all three albedo fields together with a bounded cascade model for the τ-field are given in the first four columns of Table I.) For clarity and to distinguish R_{MC} from R_{NIP}, the differences $R_{MC} - R_{IP}$ and $R_{MC} - R_{NIP}$ are also plotted. Having the same spatial mean, the standard deviation of $R_{MC} - R_{NIP}$ is three to four times smaller than of its $R_{MC} - R_{IP}$ counterpart. In particular, the average relative error (in %) between $R_{MC} - R_{IP}$ is 6.3% while between $R_{MC} - R_{NIP}$ is only 1.6%, which is not much larger than

the level of MC noise (0.5%). Note that the accuracy of NIPA is not very sensitive to the choice of η (from 0.05 to 0.25) and α (from 0.5 to 1.0): the values of $\eta \approx 0.22$ km [as estimated by (4)] and $\alpha = 0.5$ (as estimated in [15]) yield the average relative error 1.9%, which is still more than three times smaller than its $R_{MC} - R_{IP}$ counterpart.

Fig. 6(c) illustrates the energy spectra (1) averaged over two realizations. As schematically plotted in Fig. 1, IPA exhibits scale-invariance over the whole range of scales from 25 m to 13 km. Because of convolution product (6), both R_{NIP} and R_{MC} have the same energy spectra (except the small-scale differences that are caused by MC noise). Finally, both NIPA and IPA albedos are plotted versus MC albedo on a scatter

TABLE I
SOME STATISTICS OF THREE ALBEDO FIELDS AND THREE OPTICAL DEPTH FIELDS. ALL STATISTICS ARE AVERAGED OVER TWO REALIZATIONS. CLOUD MODEL, SCATTERING AND ILLUMINATION CONDITIONS ARE THE SAME AS IN FIG. 6(a) AND (b). ALBEDO FIELDS ARE PLOTTED IN FIG. 6(a) AND (b); THEIR HISTOGRAMS ARE IN FIG. 12(b), (d), AND (f). THE "TRUE" OPTICAL DEPTH FIELD (ONE REALIZATION) IS PLOTTED IN FIG. 8; ITS HISTOGRAM IS IN FIG. 12(a). HISTOGRAMS OF THE RETRIEVED OPTICAL DEPTH FIELDS ARE IN FIG. 12(c) AND (e)

	MC albedo	IPA albedo	NIPA albedo	τ_{true}	τ_{ret} (IPA)	τ_{ret} (NIPA)
min	0.271	0.189	0.258	3.307	4.871	4.194
max	0.761	0.792	0.741	40.333	33.964	44.272
mean	0.500	0.499	0.499	13	12.831	13.061
std deviat.	0.118	0.129	0.118	6.499	5.963	6.702

plot [Fig. 6(d)] for each of the 2×1024 pixels. (For clarity, R_{IP} is shifted by -0.2 in the vertical direction.) We see that the R_{NIP} points are concentrated along the diagonal showing a good agreement with MC. Note that the CPU time for the calculation of R_{NIP} was about 2500 shorter than for R_{MC}.

For high solar elevations, direct NIPA applies not only to albedo but also to nadir-viewing radiance. As an example, in Fig. 7(a) the MC nadir radiances for C1 clouds [31] with a realistic phase function [32] are shown for the same realization of 1-D bounded model as in Fig. 6(a). The appropriate NIPA has similar to the albedo fields η (≈ 0.12 km) but smaller α (≈ 0.24). This is understandable: because of an additional angular integration, the small-scale behavior of albedos is smoother than that of radiances [15], [16]. Similar to Fig. 6(d), Fig. 7(b) illustrates a scatter-plot of IPA and NIPA versus MC. The improvement of NIPA with respect to IPA is obvious.

Finally, we note that the performance of NIPA deteriorates substantially with the decrease of solar zenith angle θ_0. As mentioned above, the correction factor G is independent of solar angle. All solar angle dependence of the NIPA is concentrated in the IPA, which is insensitive to the pixel-by-pixel correlation. As a result, R_{NIP}, being a convolution product of R_{IP} and G, does not distinguish between two different azimuthal angles φ_0. However, the low-sun albedo is highly affected by φ_0. Fig. 8 illustrates two R_{MC} fields with $\varphi_0 = 0°$ and $\varphi_0 = 180°$ together with R_{IP} for $\theta_0 = 60°$. Optical depth is added for reference. We see that, while the domain-averaged values are almost identical, there are huge differences in individual pixels caused by optical shadowing. The R_{IP}, even smoothed (as R_{NIP}) to have the same energy spectrum as R_{MC}, is unable to follow pixel-by-pixel variability in R_{MC}.

A way to improve NIPA for low solar angles is to use a modified IPA with a source function based on three-dimensional (3-D) computations for the direct solar beam [10]. The new "3-D direct-beam IPA" will take care of the horizontal variations in the optical depth depending on the direction of a solar beam; its convolution with a simple approximation of the radiative transfer Green function will add the required smoothness. This should improve the total performance of NIPA for low sun. In this paper, we are not yet ready to discuss the details of the proposed modification.

To summarize, the direct NIPA, as a convolution of the IPA and the radiative transfer Green function, works well for high solar angles ($\theta_0 \leq 30°$). It improves the performance of IPA for a negligible additional computational cost using FFT. The standard deviation of the differences between MC and NIPA is typically three to four times smaller than that of MC and IPA.

Taking into account the computational cost of MC calculations, the direct NIPA is an accurate and efficient substitute of MC for both fluxes computations as well as radiances for high enough sun. However, for low solar angles ($\theta_0 \geq 60°$), the direct NIPA in its present form, while producing the same smoothness as its MC counterpart, is unable to match MC reflectance for individual pixels.

V. NONLOCAL INDEPENDENT PIXEL APPROXIMATION: THE INVERSE PROBLEM

We now set up the inverse problem of retrieving the τ-field from the R_{MC}-field. There are two main steps in the retrieval: first, we retrieve R_{IP} from (6) assuming that the approximate Green function G is known and that $R_{\mathrm{MC}}(\boldsymbol{x}) \approx R_{\mathrm{NIP}}(\boldsymbol{x})$; second, we use a look-up table to estimate τ from R_{IP}. Because of the one-to-one connection between τ and R_{IP}, the last step is trivial; so we will focus on inverting (6), i.e., solving the equation

$$R_{\mathrm{MC}}(\boldsymbol{x}) = G(\alpha, \eta; \boldsymbol{x}) * R_{\mathrm{IP}}(\boldsymbol{x}) \tag{8}$$

where R_{IP} is unknown.

Note that the deconvolution operation is a typical "ill-posed" problem. Indeed, all we know about (8) is that, if $R_{\mathrm{MC}} \equiv R_{\mathrm{NIP}}$ and $R_{\mathrm{IP}}^{(\mathrm{ex})}$ is the exact solution of (6), then the solution of (8) will be $R_{\mathrm{IP}} \equiv R_{\mathrm{IP}}^{(\mathrm{ex})}$. In general, one can write

$$R_{\mathrm{MC}}(\boldsymbol{x}) = R_{\mathrm{NIP}}(\boldsymbol{x}) + \varepsilon(\boldsymbol{x}) \tag{9}$$

where ε is the small difference between MC and NIPA fields. Furthermore, the convolution product in (8) is best done in Fourier space

$$\tilde{R}_{\mathrm{MC}}(\boldsymbol{k}) = \tilde{G}(\boldsymbol{k})\tilde{R}_{\mathrm{IP}}(\boldsymbol{k}). \tag{10}$$

Then, from (9) and (10) we have

$$\tilde{R}_{\mathrm{IP}}(\boldsymbol{k}) = \frac{\tilde{R}_{\mathrm{MC}}(\boldsymbol{k})}{\tilde{G}(\boldsymbol{k})} = \frac{\tilde{R}_{\mathrm{NIP}}(\boldsymbol{k})}{\tilde{G}(\boldsymbol{k})} + \frac{\tilde{\varepsilon}(\boldsymbol{k})}{\tilde{G}(\boldsymbol{k})}. \tag{11}$$

Applying the inverse Fourier transform to both sides of (11), we obtain

$$
\begin{aligned}
R_{\mathrm{IP}}(\boldsymbol{x}) &= \frac{1}{4\pi^2} \int \frac{\tilde{R}_{\mathrm{NIP}}(\boldsymbol{k})}{\tilde{G}(\boldsymbol{k})} \exp[i(\boldsymbol{k}, \boldsymbol{x})]\, d\boldsymbol{k} \\
&\quad + \frac{1}{4\pi^2} \int \frac{\tilde{\varepsilon}(\boldsymbol{k})}{\tilde{G}(\boldsymbol{k})} \exp[i(\boldsymbol{k}, \boldsymbol{x})]\, dk \\
&= R_{\mathrm{IP}}^{(\mathrm{ex})}(\boldsymbol{x}) + \frac{1}{4\pi^2} \int \frac{\tilde{\varepsilon}(\boldsymbol{k})}{\tilde{G}(\boldsymbol{k})} \exp[i(\boldsymbol{k}, \boldsymbol{x})]\, d\boldsymbol{k} \tag{12}
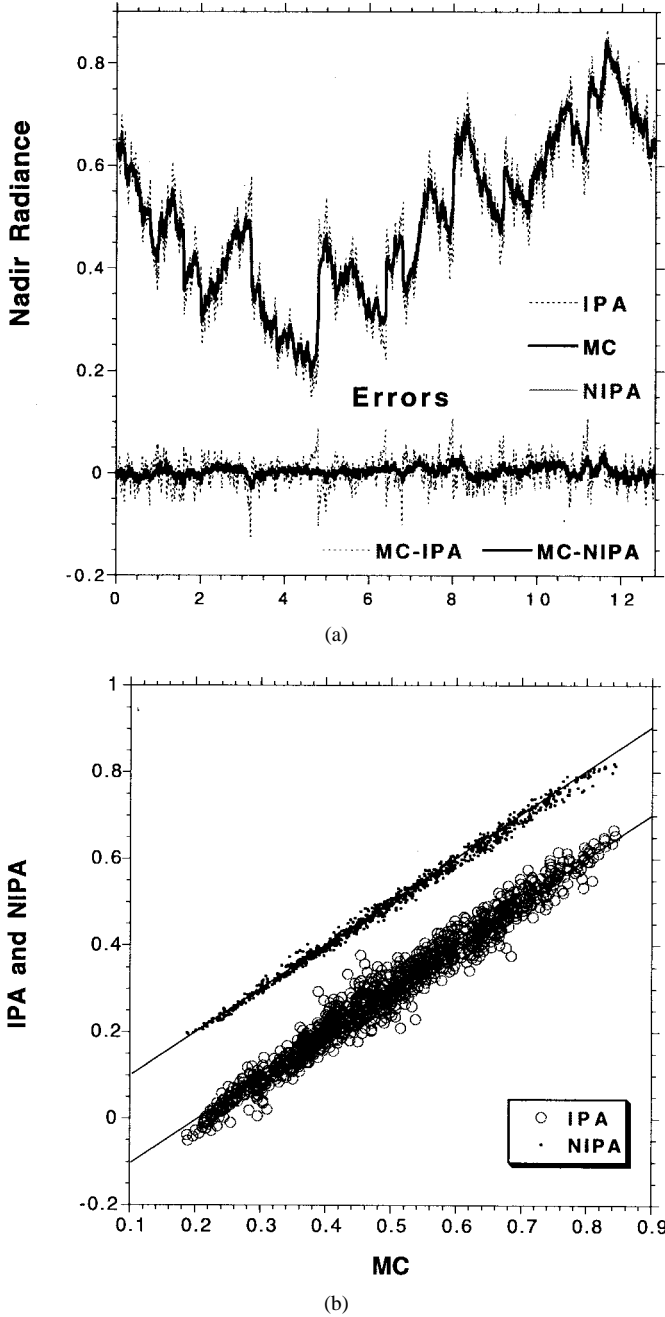\end{aligned}
$$

(a)

(b)

Fig. 7. IPA, MC and NIPA for cloud nadir radiances. (a) Cloud model and illumination conditions are the same as in Fig. 6(a). Scattering is determined by a realistic phase function specified in [32] for C1 clouds defined in [31]. Nadir radiance is used instead of albedo. To reach a less than 1% level of MC noise for the nadir radiance with a strong forward-peaked phase function, 10^9 photons were irradiated [this is five times more photons than for albedo and a Henyey–Greenstein phase function shown in Figs. 3(b), 6(a), 6(b) and 8]. The NIPA nadir radiance is computed using $\eta = 0.125$ km, $\alpha = 0.24$. (b) Scatter plot of IPA and NIPA nadir radiances versus their MC counterpart. For clarity, IPA results are shifted down by 0.2. Note a good agreement between NIPA and MC.

where $(\boldsymbol{k}, \boldsymbol{x}) = k_1 x_1 + k_2 x_2$, and $R_{\mathrm{IP}}^{(\mathrm{ex})}$ is the exact solution of (6). Note that the last integral in (12) is unstable. First of all, since both Fourier transforms $\tilde{\varepsilon}(\boldsymbol{k})$ and $\tilde{G}(\boldsymbol{k}) \rightarrow 0$ as $|\boldsymbol{k}| \rightarrow \infty$, the inverse Fourier transform of their ratio does not necessarily exist. Second, even if the last integral exists, the effect of large $|\boldsymbol{k}|$'s can make this integral quite large;
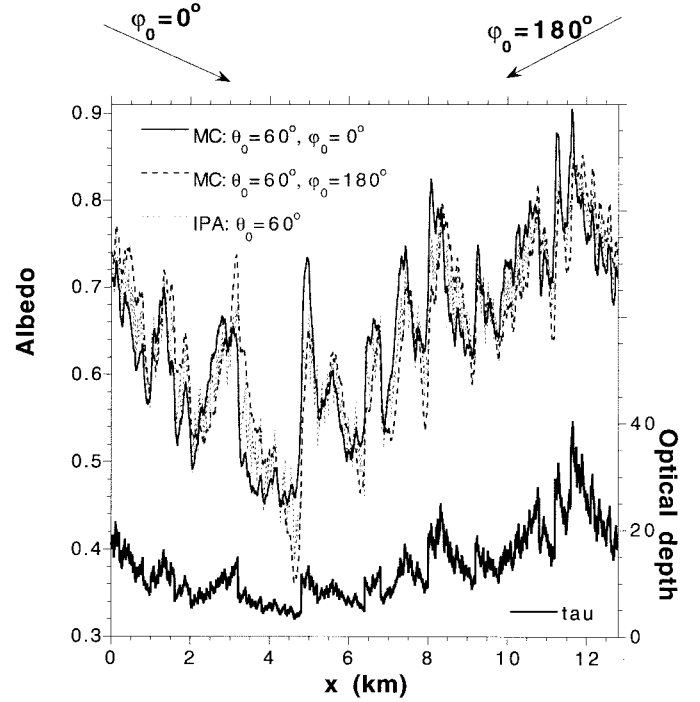

Fig. 8. IPA, and MC albedos for two different azimuthal angles. Cloud model and scattering are the same as in Fig. 6(a). Horizontal distribution of optical depth is given for reference. Solar zenith angle $\theta_0 = 60°$. MC results correspond to two azimuthal angles: $\varphi_0 = 0°$ (illumination from the left) and $\varphi_0 = 180°$ (illumination from the right). IPA results are φ_0-independent. Note sharp fluctuations that correspond to cloud optical shadows; their locations strongly depend on the azimuthal direction of the direct solar beam. The results of IPA are mostly between of those by MC. The results of NIPA are not shown since they are based on the IPA and unable to match those of MC.

in essence, the "noise" ε is amplified by the high-pass filter described by $1/\tilde{G}(\boldsymbol{k})$. As a result, $R_{\mathrm{IP}}(\boldsymbol{x})$ can be very far from the exact solution $R_{\mathrm{IP}}^{(\mathrm{ex})}(\boldsymbol{x})$. In other words, small differences between R_{MC} and R_{NIP} lead to unpredictable differences between R_{IP} and $R_{\mathrm{IP}}^{(\mathrm{ex})}$; thus the optical depth field cannot be accurately retrieved.

It follows from the above arguments that, in order to get a stable solution of (8), we at least have to remove artificially the effect of large harmonics in (12). This is equivalent to the low-pass filtering, or small-scale smoothing. Let us introduce an even function $f(\gamma; \boldsymbol{k})$ that is defined for any $\gamma \geq 0$ with the following main properties [35]:

$$f(\gamma; \boldsymbol{k}) \rightarrow 0 \text{ as } |\boldsymbol{k}| \rightarrow \infty \text{ for any } \gamma > 0 \qquad (13a)$$

$$f(\gamma; \boldsymbol{k}) \rightarrow 1 \text{ as } \gamma \rightarrow 0. \qquad (13b)$$

We now seek the solution of (8) in the form of

$$R_{\mathrm{IP}}(\gamma; \boldsymbol{x}) = \frac{1}{4\pi^2} \int \frac{\tilde{R}_{\mathrm{MC}}(\boldsymbol{k})}{\tilde{G}(\boldsymbol{k})} f(\gamma; \boldsymbol{k}) \exp[i(\boldsymbol{k}, \boldsymbol{x})] \, d\boldsymbol{k}. \qquad (14)$$

Function $f(\gamma; \boldsymbol{k})$ will "stabilize" our solution. Indeed, because of (13a), it removes the effect of large $|\boldsymbol{k}|$'s, and due to (13b) it converges to the unstable "solution" as $\gamma \rightarrow 0$. As a simple independent of G "stabilizer" $f(\gamma; \boldsymbol{k})$, one can take

$$f(\gamma; \boldsymbol{k}) = \exp(-\gamma^2 |\boldsymbol{k}|^2) \qquad (15a)$$
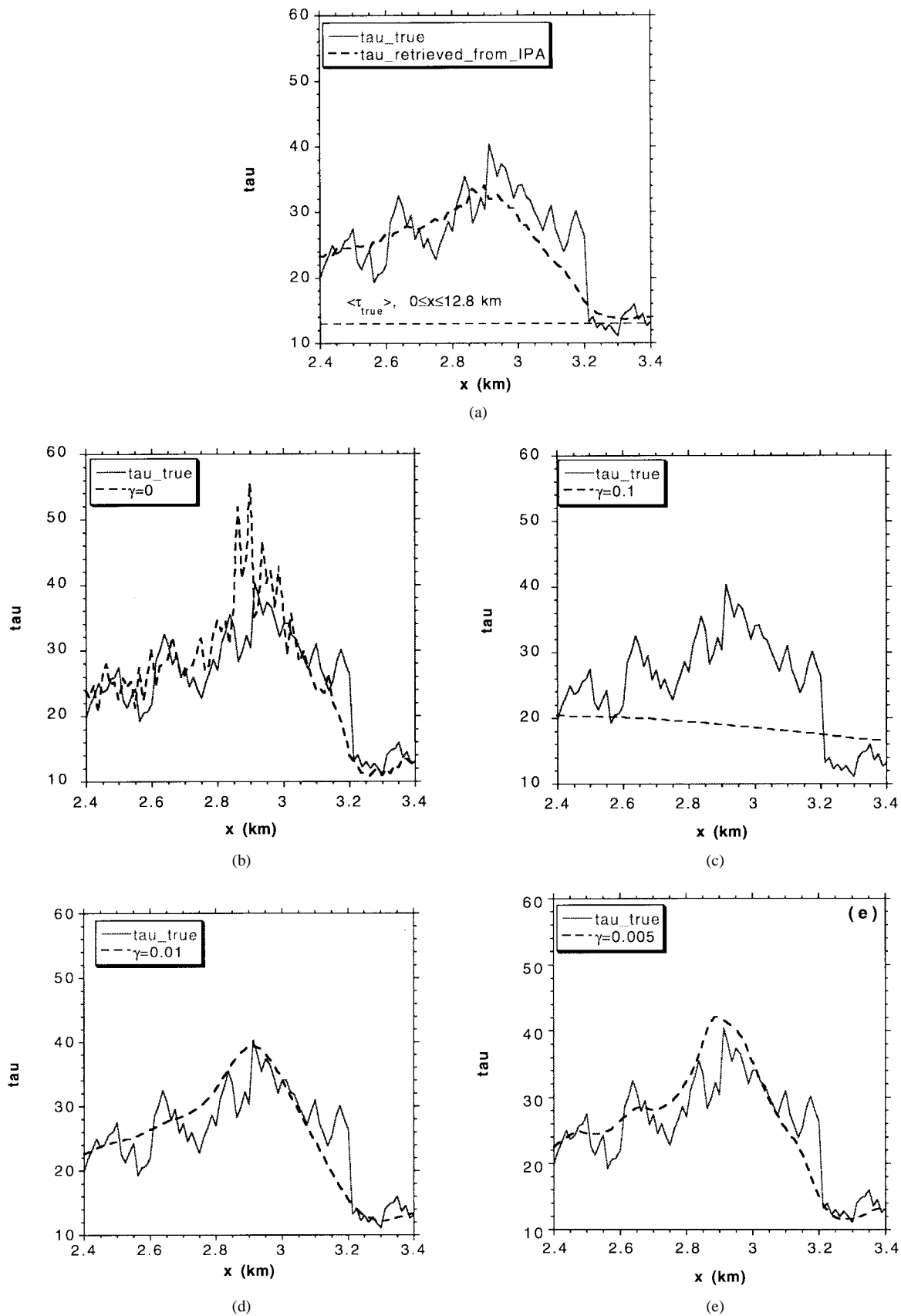
which satisfies (13a) and (13b).

Fig. 9.   A 1-km fragment of a large optical thickness retrieval. (a) IPA-retrieved τ-field together with "true" τ from the bounded cascade model [the same one as used in Fig. 6(b)]. Note that because of radiative smoothing the retrieved field is much less variable than the original one. (b) NIPA-retrieved τ-field without regularization. Note that most retrieved τ's show errors larger than for inverse IPA. (c) NIPA retrieved τ-field with regularization parameter $\gamma = 0.1$. The retrieved curve is even smoother than for IPA. (d) NIPA retrieved τ-field with regularization parameter $\gamma = 0.01$. The retrieved curve is still too smooth. (e) NIPA retrieved τ-field with regularization parameter $\gamma = 0.005$, which is the optimal value in the sense that it minimizes the standard deviation between τ_{true} and τ_{ret}. Note that the resulting τ-field is again smoother than "true" τ; however, it is a much better approximation than the one in (b).
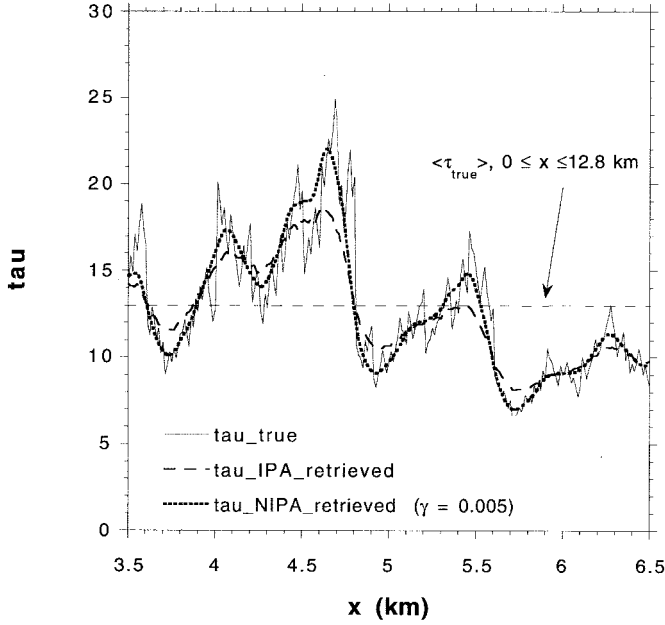
Fig. 10. A 3-km fragment of optical thickness retrieval (next to the one in Fig. 9). "True" τ is plotted together with IPA and NIPA retrievals. Note that the NIPA retrieval is much better than its IPA counterpart. From the other side, the regularization parameter $\gamma = 0.005$ being optimal for the whole field, is not optimal for this 3-km fragment. Decreasing γ, one gets a rougher—and closer to "true"—retrieved τ-field.

Fig. 11. The inverse NIPA and IPA; the effect of NIPA regularization in a "retrieved" versus "true" scatter plot. Optical depths are retrieved from the 1-D nadir radiances for C1 clouds plotted in Fig. 7. The "true" optical depth is plotted in Fig. 8. Note how increasing the value of γ eliminates the outliers at large τ. For this retrieval, the regularization parameter $\gamma = 0.001$ is found to be optimal. For clarity, IPA retrieved τ-field is shifted down by 20.

From the other side, it can be shown [35] that for any $\gamma > 0$, there is a function

$$f(\gamma; \boldsymbol{k}) = \frac{|\tilde{G}(\boldsymbol{k})|^2}{|\tilde{G}(\boldsymbol{k})|^2 + \gamma(1 + |\boldsymbol{k}|^2)} \qquad (15\text{b})$$

that minimizes the integral

$$\int_{\text{all}\,\boldsymbol{x}} \left([R_{\text{MC}}(\boldsymbol{x}) - G(\alpha, \eta; \boldsymbol{x}) * R_{\text{IP}}(\gamma; \boldsymbol{x})]^2 \right.$$
$$\left. + \gamma \left\{ R_{\text{IP}}(\gamma; \boldsymbol{x})^2 + \sum_{i=1}^{2} \left[\frac{\partial R_{\text{IP}}(\gamma; \boldsymbol{x})}{\partial x_i} \right]^2 \right\} \right) d\boldsymbol{x}. \quad (16)$$

It is easy to check that (15b) satisfies (13a) and (13b). Substituting (15b) into (14), we have

$$R_{\text{IP}}(\gamma; \boldsymbol{x}) = \frac{1}{4\pi^2} \int \frac{\tilde{R}_{\text{MC}}(\boldsymbol{k})\tilde{G}(-\boldsymbol{k})}{|\tilde{G}(\boldsymbol{k})|^2 + \gamma(1 + |\boldsymbol{k}|^2)} \exp[i(\boldsymbol{k}, \boldsymbol{x})]\, d\boldsymbol{k}. \quad (17)$$

If one knows additionally the energy spectra E of both the unknown solution R_{IP} and the difference between R_{MC} and R_{NIP}, the optimal stable solution of (8) can be expressed as [35]

$$R_{\text{IP}}^{\text{opt}}(\boldsymbol{x}) = \frac{1}{4\pi^2} \int \frac{\tilde{R}_{\text{MC}}(\boldsymbol{k})\tilde{G}(-\boldsymbol{k})}{|\tilde{G}(\boldsymbol{k})|^2 + \dfrac{E_{R_{\text{MC}} - R_{\text{NIP}}}(\boldsymbol{k})}{E_{R_{\text{IP}}}(\boldsymbol{k})}}$$
$$\cdot \exp[i(\boldsymbol{k}, \boldsymbol{x})]\, d\boldsymbol{k} \qquad (18)$$

where $E_{R_{\text{IP}}}$ and $E_{R_{\text{MC}} - R_{\text{NIP}}}$ are energy spectra of R_{IP}, and $R_{\text{IP}} - R_{\text{MC}}$, respectively. Note that (18) coincides with the so-called optimal Wiener filter [36]. More sophisticated
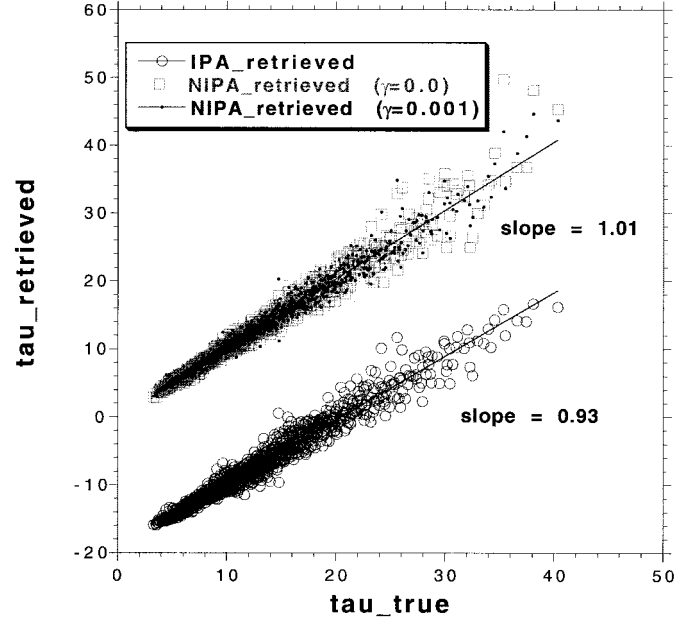
techniques of stabilizing the solutions of ill-posed problems and defining the regularization parameter γ in (17) are given, for instance, in [35].

To demonstrate the effect of the regularization parameter γ in (15a), we plotted in Fig. 9, a 1-km fragment of the retrieval with different γ's. If $\gamma = 0$ (no stabilization), the retrieved optical thickness τ_{ret} is quite erratic [Fig. 9(b)]; large values of τ_{ret} for several pixels exceed τ_{true} over 100%. To better understand physical reasons of these uncertainties, note that the smoothing kernel G defined in (5) uses a parameter η from (4), which is determined entirely by the average value of optical thickness $\langle \tau \rangle$. For regions with optical thicknesses several times larger than $\langle \tau \rangle$, the local radiative smoothing scale $\eta_{\text{loc}} < \eta$. For those pixels, R_{NIP} is smoother than its R_{MC} counterpart. As a result, the inverse NIPA yields rougher R_{IP} and therefore more variable τ_{ret}. Mathematically, this follows from the unpredictably large values at high frequency in the last integral in (12).

Fig. 9(c) and (d) demonstrate the effect of large γ's. As we see, the resulting τ_{ret}-field is much smoother than τ_{true}; for $\gamma = 0.1$, τ_{ret} is even smoother than τ retrieved from the simplest IPA plotted in Fig. 9(a). Fig. 9(e) shows τ_{ret} with $\gamma = 0.005$, which minimizes $\sigma_{\tau_{\text{true}} - \tau_{\text{ret}}}$. Note that the fragment shown in Fig. 9 is amongst the worst cases; the retrieval algorithm works much better for regions with close-to-average optical thicknesses. In Fig. 10 we plotted a 3-km fragment (next to the one in Fig. 9) that has τ from 5 to 25 (recall that $\langle \tau \rangle = 13$). We can clearly see how NIPA-retrieved τ's improve on those retrieved from IPA.

The scatter plot in Fig. 11 shows the effect of stabilizing the inverse NIPA and compares it with inverse IPA. Both methods retrieve optical depth from the nadir radiances for C1 clouds
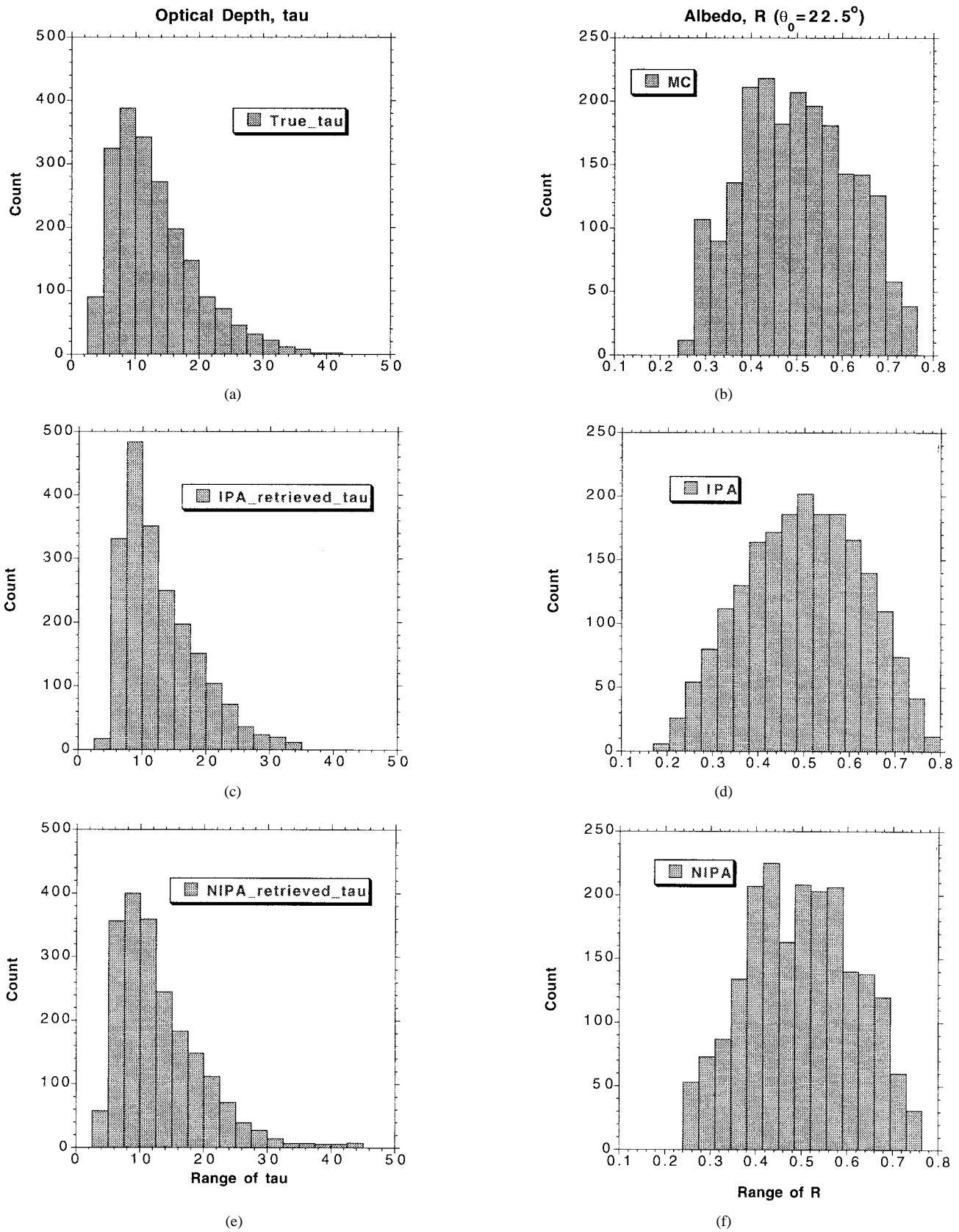
Fig. 12.   The histograms of MC, IPA, and NIPA albedos together with "true" and retrieved optical depths. Two realizations plotted in Fig. 6(a) and (b) are used. (a) A "true" optical depth to be retrieved. (b) R_{MC}. (c) Optical depth retrieved from R_{MC} using inverse IPA. (d) R_{IP}. (e) Optical depth retrieved from R_{MC} using inverse NIPA. (f) R_{NIP}.

plotted in Fig. 7(a). As mentioned above, by changing γ, we affect primarily the retrieval of large τ's. To quantitatively characterize retrieval, we use a standard deviation of the differences between τ_{true} and τ_{ret}. For the above retrieval, we have $\sigma_{\tau_{\text{true}}-\tau_{\text{ret}}} = 1.30$ for NIPA without regularization, 1.29 for IPA and 1.07 for NIPA with regularization. Also note that the least-square fit for NIPA yields a slope of 1.01, which is far better than the one obtained for IPA, which is 0.93.

Finally, we use histograms (Fig. 12) to illustrate both methods. Some statistics of all six fields (three albedo fields and three optical depth fields) are given in Table I. Fig. 12(a) shows a histogram of a bounded model, which is close to the log–normal one. Fig. 12(b), (d), and (f) illustrate histograms of R_{MC}, R_{IP}, and R_{NIP}, respectively. We see that because of photon horizontal fluxes, both R_{MC} and R_{NIP} have irregular shapes; the histogram of R_{IP} has a regular shape, which is the result of a one-to-one transformation of each bin in Fig. 12(a). As shown in Table I, R_{IP} has the largest range (from 0.19–0.79), while the ranges of R_{NIP} and R_{MC} are very close (from 0.26–0.74 and from 0.27–0.76, respectively.) As a result, standard deviation σ_{IP} is almost 10% larger than its NIPA and MC counterparts. Fig. 12(c) and (e) illustrate histograms for two τ's retrieved from R_{MC}. It is not surprising, that the range of the IPA-retrieved τ is smaller; the IPA is unable to retrieve large τ's and completely misses the long tail of the τ-pdf. As shown in Table I, its mean value and standard deviation are also smaller. The NIPA-retrieved optical depth slightly overestimates the range of τ; however, its mean value and standard deviation are closer to those of τ_{true} than their IPA counterparts.

To summarize, even a simple regularization (14) and (15a) of the ill-posed problem (8) improves the retrieval of optical depth with respect to IPA. However, the inverse NIPA, in its present form, exhibits less accuracy than its direct counterpart. There is a hope that a more complicated technique with a stabilizer $f(\gamma; k)$ as a function of G [see (15b), (17), and (18)] will substantially improve optical depth retrieval.

VI. GENERAL SUMMARY AND DISCUSSION

Scale-by-scale analysis of the variability of both internal cloud structure and the associated radiation fields is a powerful instrument for studying the smoothing effect of multiple scattering. Starting with a scale-invariant model of the horizontal distribution of optical depth (Fig. 2), we showed that while IPA (just standard plane-parallel radiative transfer on a pixel-by-pixel basis) preserves scale-invariance, MC yields two distinct scaling regimes. Large-scale fluctuations, to a first approximation, are similar to those of cloud structure but the small-scale variability is essentially weaker (Fig. 1). This is due to photon horizontal transport, which is strong enough to smooth the small-scale fluctuations of optical depth.

Using the diffusion approximation, the radiative smoothing scale η can be estimated as a measure of the range where net horizontal fluxes arise [16]. The scale η is proportional to the harmonic mean of cloud depth and photon transport mean free path (4). A statistically robust analysis of LANDSAT cloud scenes [Fig. 4(a) and (b)] not only confirms this theoretical

result but also indicates a way to improve IPA. Indeed, Fig. 1 shows that, if we are able to define a simple operation on the R_{IP} field that bends its spectrum $E(k)$ around the radiative smoothing scale η, then we have a method statistically comparable with MC. A convolution product (6) between IPA and an approximate Green function for radiative transfer (5) is such an operation. Since, in contrast to IPA, the new method takes into account optical properties of neighboring pixels, we called it the "nonlocal" IPA or NIPA. Figs. 3, 6, and 7 illustrate NIPA and compare it with the traditional IPA.

To retrieve cloud optical thickness from an unknown R_{IP} corresponding to a given R_{MC}, we developed the inverse NIPA. Instead of a simple deconvolution of (8), which is a typical ill-posed problem, we used a regularization (14) that enables us to get a *stable* solution of (8). Fig. 10 illustrates how the (too-smooth) τ-field retrieved directly from IPA can be improved by the NIPA retrieval. Note that, since the radiative smoothing scale η depends only on average optical thickness $\langle\tau\rangle$, both direct and inverse NIPA work better for optical thicknesses not too far from the average value $\langle\tau\rangle$. Indeed, in a region of large τ, the "local" radiative smoothing scale is smaller than η. As a result, direct NIPA (being a convolution) smooths this neighborhood more than necessary; conversely, inverse NIPA yields τ's that are too rough.

Another weak point of NIPA is related to the compounded effects of cloud edges and oblique illumination (Fig. 8). Since both IPA and NIPA are independent of solar azimuthal angle, the shadowing effect of cloud edges is not taken into account. Consequently, NIPA violates the principle of directional reciprocity [37], and the retrieved optical thickness from the illuminated side will be overestimated while the one from the shadowed side will be underestimated. To generalize NIPA for oblique illumination, we can use the so-called "3-D direct-beam IPA," which is a modification of IPA, by using the results of 3-D computations for the direct solar beam [10]. For broken cloudiness we have to adapt the definition of radiative smoothing to variable sun angles and use a more sophisticated approximation of the radiative transfer Green function.

In spite of the limitations listed above, NIPA proves to be a substantial improvement over the standard IPA. On the one hand, it allowed us to reproduce the observed two-point statistics of high-resolution satellite radiances. On the other hand, the NIPA-retrieved one-point distribution of cloud optical thickness is quite realistic, leading in particular to similar mean and standard deviation as for the actual cloud optical thickness. The simplicity and computational efficiency of NIPA enables it to be used in high-resolution satellite imagery retrieval algorithms for cloud optical properties [13], [38].

Finally, we note that another application of the fundamental smoothing scale (4) found in marine stratocumulus is in active rather than passive cloud remote sensing. The idea is to directly measure the brightness distribution in the spot created by pencil-beam illumination of a cloud. One can set up a pulsed-lidar experiment in which the measured spot profile is combined with the distribution of photon arrival times to infer both the cloud's geometrical and optical thicknesses, as well as information on cloud structure, at $\approx 2\eta \approx 0.5$ km resolution [16], [39].

REFERENCES

[1] W. B. Rossow, L. C. Garder, and A. A. Lacis, "Global, seasonal cloud variations from satellite radiance measurements—Part I: Sensitivity of analysis," *J. Climate,* vol. 2, pp. 419–458, 1989.

[2] W. B. Rossow and R. A. Schiffer, "ISCCP cloud data products," *Bull. Amer. Meteor. Soc.,* vol. 72, pp. 2–20, 1991.

[3] T. Nakajima and M. D. King, "Determination of the optical thickness and effective particle radius of clouds from reflected solar radiation measurements—I: Theory," *J. Atmos. Sci.,* vol. 47, pp. 1878–1893, 1990.

[4] P. Minnis, P. W. Heck, D. F. Young, C. W. Fairall, and J. B. Snider, "Stratocumulus cloud properties derived from simultaneous satellite- and island-based measurements during FIRE," *J. Appl. Meteor.,* vol. 31, pp. 317–339, 1992.

[5] S. Platnick and S. Twomey, "Determining the susceptibility of cloud albedo to changes in droplet concentration with the advanced very high resolution radiometer," *J. Appl. Meteor.,* vol. 33, pp. 334–347, 1994.

[6] R. Pincus, M. Szczodrak, J. Gu, and P. Austin, "Uncertainty in cloud optical depth estimates made from satellite radiance measurements," *J. Climate,* vol. 8, pp. 1453–1462, 1995.

[7] N. G. Loeb and R. Davies, "Observational evidence of plane parallel model biases: Apparent dependence of cloud optical depth on solar zenith angle," *J. Geophys. Res.,* vol. 101, pp. 1621–1634, 1996.

[8] Harshvardan, B. A. Wielicki, and K. M. Ginger, "The interpretation of remotely sensed cloud properties from a model parameterization perspective," *J. Climate,* vol. 7, pp. 1987–1998, 1994.

[9] R. F. Cahalan, W. Ridgway, W. J. Wiscombe, T. L. Bell, and J. B. Snider, "The albedo of fractal stratocumulus clouds," *J. Atmos. Sci.,* vol. 51, pp. 2434–2455, 1994.

[10] P. M. Gabriel and K. F. Evans, "Simple radiative-transfer methods for calculating domain-averaged solar fluxes in inhomogeneous clouds," *J. Atmos. Sci.,* vol. 53, pp. 858–877, 1996.

[11] H. W. Barker, "A parameterization for computing grid-averaged solar fluxes for inhomogeneous marine boundary layer clouds—Part 1: Methodology and homogeneous biases," *J. Atmos. Sci.,* vol. 53, pp. 2289–2303, 1996.

[12] H. W. Barker, B. A. Wielicki, and L. Parker, "A parameterization for computing grid-averaged solar fluxes for inhomogeneous marine boundary layer clouds—Part 2: Validation using satellite data," *J. Atmos. Sci.,* vol. 53, pp. 2304–2316, 1996.

[13] L. H. Chambers, B. A. Wielicki, and K. F. Evans, "On the accuracy of the independent pixel approximation for satellite estimates of oceanic boundary layer cloud optical depth," *J. Geophys. Res.*, vol. 102, pp. 1779–1794, 1997.

[14] R. F. Cahalan, W. Ridgway, W. J. Wiscombe, S. Golmer, and Harshvardan, "Independent pixel and Monte Carlo estimates of stratocumulus albedo," *J. Atmos. Sci.,* vol. 51, pp. 3776–3790, 1994.

[15] A. Marshak, A. Davis, W. J. Wiscombe, and R. F. Cahalan, "Radiative smoothing in fractal clouds," *J. Geophys. Res.,* vol. 100, pp. 26 247–26 261, 1995.

[16] A. Davis, A. Marshak, R. Cahalan, and W. Wiscombe, "The LANDSAT scale-break in stratocumulus as a three-dimensional radiative transfer effect, implications for cloud remote sensing," *J. Atmos. Sci.,* vol. 54, pp. 241–260, 1997.

[17] G. A. Titov, "Radiative horizontal transport and absorption by stratocumulus clouds," to be published.

[18] K. F. Evans, "The spherical harmonic discrete ordinate method: Application to 3D radiative transfer in boundary layer clouds," in *Proc. IRS'96: Current Problems Atmospheric Radiation,* W. Smith and K. Stamnes, Eds. Hampton, VA: Deepak, 1997, pp. 143–146.

[19] R. F. Cahalan and J. B. Snider, "Marine stratocumulus structure," *Remote Sens. Environ.,* vol. 28, pp. 95–107, 1989.

[20] R. F. Cahalan, "Bounded cascade clouds: Albedo and effective thickness," *Nonlin. Proc. Geophys.,* vol. 1, pp. 156–167, 1994.

[21] A. Davis, A. Marshak, W. Wiscombe, and R. Cahalan, "Multifractal characterizations of nonstationarity and intermittency in geophysical fields, observed, retrieved or simulated," *J. Geophys. Res.,* vol. 99, pp. 8055–8072, 1994.

[22] ——, "Scale-invariance of liquid water distributions in marine stratocumulus, Part I—Spectral properties and stationarity issues," *J. Atmos. Sci.,* vol. 53, pp. 1538–1558, 1996.

[23] W. Wiscombe, A. Davis, A. Marshak, and R. Cahalan, "Scale-invariance, nonstationarity and intermittency in the structure of cloudiness," in *Proc. 4th Atmospheric Radiation Measurement (ARM) Sci. Team Meeting,* Charleston, SC, Feb. 28–Mar. 3, 1994, U.S. Dept. Energy, pp. 11–14.

[24] A. S. Monin and A. M. Yaglom, *Statistical Fluid Mechanics.* Boston, MA: MIT Press, 1975, vol. 2, p. 683.

[25] D. Schertzer and S. Lovejoy, "Physical modeling and analysis of rain clouds by anisotropic scaling multiplicative processes," *J. Geophys. Res.,* vol. 92, pp. 9693–9714, 1987.

[26] A. Marshak, A. Davis, R. Cahalan, and W. Wiscombe, "Bounded cascade models as nonstationary multifractals," *Phys. Rev. E,* vol. 49, pp. 55–69, 1994.

[27] S. Pecknold, S. Lovejoy, and D. Schertzer, "The morphology and texture of anisotropic multifractals using generalized scale invariance," in *Stochastic Models in Geosystems,* S. Molchanov and W. Woyinski, Eds., IMA. New York: Springer-Verlag, 1997, pp. 269–311.

[28] K. Stamnes, S.-C. Tsay, W. J. Wiscombe, and K. Jayaweera, "Numerically stable algorithm for discrete-ordinates-method radiative transfer in multiple scattering and emitting layered media," *Appl. Opt.,* vol. 27, pp. 2502–2512, 1988.

[29] A. Marshak, A. Davis, W. Wiscombe, and G. Titov, "The verisimilitude of the independent pixel approximation used in cloud remote sensing," *Remote Sens. Environ.,* vol. 52, pp. 71–78, 1995.

[30] G. Marchuk, G. Mikhailov, M. Nazaraliev, R. Darbinjan, B. Kargin, and B. Elepov, *The Monte Carlo Methods in Atmospheric Optics.* New York: Springer-Verlag, 1980, p. 208.

[31] D. Deirmendjian, *Electromagnetic Scattering on Spherical Polydispersions.* New York: Elsevier, 1969, 292 pp.

[32] R. Garcia and C. Siewert, "Benchmark results in radiative transfer," *Transp. Theory Stat. Phys.,* vol. 14, pp. 437–484, 1985.

[33] S. Lovejoy, D. Schertzer, P. Silas, Y. Tessier, and D. Lavallee, "The unified scaling model of atmospheric dynamics and systematic analysis of scale invariance in cloud radiances," *Ann. Geophysicae,* vol. 11, pp. 119–127, 1993.

[34] A. Davis and A. Marshak, "Cloud responses from CW and pulsed lasers as Green's functions: What do they tell us? & can we measure them?" in *Proc. Int. Workshop Multiple Scattering Lidar Experiments (MUSCLE 8),* D.R.E.V., Valcartier, P.Q., Canada, Mar. 4–6 1996, pp. 67–71.

[35] A. N. Tikhonov, *Solutions of Ill-Posed Problems.* New York: Winston, 1977, p. 258.

[36] L. R. Rabiner and B. Gold, *Theory and Application of Digital Signal Processing.* Englewood Cliffs, NJ: Prentice-Hall, 1975.

[37] R. Davies, "Spatial autocorrelation of radiation measured by the earth radiation budget experiment: Scene inhomogeneity and reciprocity violation," *J. Geophys. Res.,* vol. 99, pp. 20 879–20 887, 1994.

[38] H. Barker and D. Liu, "Inferring cloud optical depths from LANDSAT data," *J. Climate,* vol. 8, pp. 2620–2630, 1996.

[39] A. Davis, D. M. Winker, A. Marshak, J. D. Spinhirne, R. F. Cahalan, S. Love, S. H. Melfi, and W. J. Wiscombe, "Retrieval of physical and optical cloud thicknesses from space-borne and wide-angle lidar," in *Proc. 18th Int. Laser Radar Conf.,* Berlin, Germany, July 22–26, 1996, pp. 193–196, 1997.

Alexander Marshak received the M.S. degree in applied mathematics from Tartu State University, Tartu, Estonia, and the Ph.D. degree in numerical analysis from the Siberian Branch of the Russian Academy of Sciences, Novosibirsk, Russia, in 1978 and 1983, respectively.

From 1978 to 1989, he was a Research Scientist at the Institute of Astrophysics and Atmospherics Physics, Tartu. He has worked at the University of Gottingen, Gottingen, Germany. He is currently a Research Scientist with the Climate and Radiation Branch of NASA Goddard Space Flight Center, Greenbelt, MD. He has been actively involved in radiative transfer in atmosphere and vegetation since 1980. Since 1991, his research interests have been in theoretical cloud radiation study and stochastic cloud modeling. Dr. Marshak was an Alexander von Humboldt Fellow from 1989 to 1991.

Anthony Davis received the M.Sc. degree in physics from the University of Montreal, Montreal, P.Q., Canada, in 1980 and the Ph.D. degree in physics from McGill University, Montreal, in 1992.

He studied and taught theoretical and observational astrophysics from 1978 to 1984, also lecturing and producing shows at the Dow Planetarium, Montreal. From 1985 to 1992, his interests shifted to computational radiative transfer in highly variable scattering/absorbing media in application to remote sensing of the atmospheric environment (specifically, aerosols then clouds). As a USRA-sponsored Visiting Scientist at NASA's Goddard Space Flight Center, Greenbelt, MD, from 1992 to 1994, he developed scale-by-scale statistical analysis techniques for geophysical signals with an emphasis on the internal structure of boundary-layer clouds. In parallel, he was applying multifractal concepts to stochastic cloud modeling. His current research interests are wavelet-based statistical characterizations of 2-D geophysical fields and analysis (as well as numerical and laboratory simulations) of remotely sensed cloud data at visible/near-IR wavelengths in both passive and active (lidar) modes. In Fall 1997, he joined the Astrophysics & Radiation Measurements group, DoE's Los Alamos National Laboratory, Albuquerque, NM.

Robert F. Cahalan received the Ph.D. in theoretical physics from University of Illinois, Urbana, in 1973.

He was an Assistant Professor of Physics at Syracuse University, Syracuse, NY, and a Visiting Scientist at the Institute of Theoretical Physics, Warsaw, Poland, during which time he published several papers in particle physics. In 1977, he turned to atmospheric sciences as a Senior Postdoctoral Fellow at the National Center for Atmospheric Research, Boulder, CO. There he published papers investigating the stability of terrestrial climate using stochastic models. In 1979, he joined the Laboratory for Atmospheres, Goddard Space Flight Center, Greenbelt, MD, where he is now Senior Research Scientist. He has recently published in several areas—fractal cloud structure and radiation, where he introduced the "IPA" and "effective thickness" approximations, empirical orthogonal functions, where he derived an "analytic noise spectrum" used to separate climate signal from noise, and the Kuwait oil fires, where he combined satellite and surface data to demonstrate the localizing influence of the subtropical inversion.

Dr. Cahalan is a member of the NASA Landsat Science Team, the DoE Atmospheric Radiation Measurement Science Team, and the DoE Unmanned Aerospace Vehicle Science Team, where he co-chairs the Radiative Fluxes Working Group.

Warren Wiscombe received the M.S. degree in physics and the Ph.D. degree in applied mathematics from the California Institute of Technology, Pasadena, in 1966 and 1970, respectively.

From 1969 to 1975, he was a Research Scientist at Systems, Science & Software, La Jolla, CA. He was a Staff Scientist at the National Center for Atmospheric Research from 1974 to 1980. He was then an Assistant Professor, Department of Applied Sciences, New York University, New York, NY, from 1980 to 1984. He is currently a Senior Research Scientist with the Climate and Radiation Branch, NASA Goddard Space Flight Center, Greenbelt, MD. He has been actively involved in radiative transfer in the atmosphere since 1970.